ISSN: 2476-6909; Modares. Mech. Eng. 2027;27(04):351-363.

Modares Mechanical Engineering

DOI: 10.48311/mme.2026.124432.83130
journal homepage: mme.modares.ac.ir

Layer-wise co-optimization of infill density and configuration in FDM-printed PLA: hierarchical effects on tensile performance

Amirali Nakhaei[1], Ali Akbari Lalaei[1], Hamed Adibi[1*], Arash Mahdavi[2]

[1] Amirkabir University of Technology, Department of Mechanical Engineering, Iran
[2] Babol Noshirvani University of Technology, Department of Mechanical Engineering, Iran

ARTICLE INFO

Article Type
Original Research

Article History
Received: October 18, 2026
Revised: November 03, 2026
Accepted: November 07, 2026
ePublished: November 14, 2026

ABSTRACT

Uniform infill strategies overlook how infill density and pattern interact across the thickness of additively manufactured polymer parts. This study examined the mechanical performance of three-zone PLA specimens, with each zone assigned an infill density (30%, 60%, or 90%) and a configuration combining pattern geometry and raster orientation. An L18 Taguchi design guided fabrication, and a general linear model quantified factor contribution. Core density was the dominant predictor of ultimate tensile strength, accounting for 54.7% of the explained variation, while core configuration contributed 7.2% ($p < 0.001$). Configuration effects depended on density: honeycomb at 0° favored strength at moderate core densities, whereas rectilinear at ±45° improved stiffness at high densities. Abrupt transitions between zones had a smaller, statistically nonsignificant effect, although smoother gradients were qualitatively associated with better strength retention. Segmented specimens exhibited tortuous crack paths and ductile post-yield behavior, unlike the brittle fracture observed in uniform solid references. The best segmented design approached reference tensile strength within 5–13%, while reducing material use by approximately 30% and printing time by 50%. Mult objective optimization yielded a composite desirability of 0.593. These findings identify core density as the primary design variable for lightweight, functionally graded FDM parts and highlight the importance of separately evaluating pattern geometry and raster orientation.

Keywords: Fused Deposition Modeling; Polylactic Acid; Multi-zone Graded Infill; Configuration–Density Co-Optimization; Tensile Properties

How to cite this article
Nakhaei A A, Akbari LaLaei A, Adibi H, Mahdavi A, Layer-wise co-optimization of infill density and configuration in FDM-printed PLA: hierarchical effects on tensile performance. Modares Mechanical Engineering; 2027;27(04):351-363.

*Corresponding author's email: hadibi@aut.ac.ir
*Corresponding ORCID ID: 0000-0002-9956-0344

Copyright© 2027, TMU Press. This open-access article is published under the terms of the Creative Commons Attribution-NonCommercial 4.0 International License which permits Share (copy and redistribute the material in any medium or format) and Adapt (remix, transform, and build upon the material) under the Attribution-NonCommercial terms.

شاپا: ۶۹۰۹-۲۴۷۶؛ مهندسی مکانیک مدرس. ۳۶۳-۳۵۱:(۰۴)۲۷؛۱۴۰۶

مهندسی مکانیک مدرس

DOI: 10.48311/mme.2026.124432.83130

صفحه اصلی مجله: mme.modares.ac.ir

بهینه‌سازی همزمان لایه‌به‌لایه چگالی و الگوی پُرشدگی در قطعات PLA چاپ‌شده به روش FDM: بررسی اثرات سلسله‌مراتبی بر رفتار کششی

امیرعلی نخعی[۱]، علی اکبری لالائی[۱]، حامد ادیبی[۱*]، آرش مهدوی[۲]

[۱] گروه مهندسی مکانیک، دانشگاه صنعتی امیرکبیر، تهران، ایران

[۲] گروه مهندسی مکانیک، دانشگاه صنعتی نوشیروانی بابل، مازندران، ایران

اطلاعات مقاله

نوع مقاله

مقاله پژوهشی

تاریخچه مقاله

دریافت: ۱۴۰۵/۰۷/۲۶

بازنگری: ۱۴۰۵/۰۸/۱۲

پذیرش: ۱۴۰۵/۰۸/۱۶

ارائه آنلاین: ۱۴۰۵/۰۸/۲۳

چکیده

راهبردهای پرکنندگی یکنواخت در ساخت افزایشی، برهم‌کنش چگالی و الگوی پرکنندگی را در ضخامت قطعات پلیمری به‌خوبی نشان نمی‌دهند. در این پژوهش، نمونه‌های PLA به سه ناحیه در راستای ضخامت تقسیم شدند و برای هر ناحیه، چگالی ۳۰، ۶۰ یا ۹۰ درصد و پیکربندی متشکل از الگو و جهت‌گیری مسیر چاپ تعیین شد. آزمایش‌ها با آرایه تاگوچی L18 طراحی و سهم عوامل با مدل خطی عمومی ارزیابی شد. چگالی ناحیه مرکزی با سهم ۵۴/۷ درصد از تغییرات تبیین‌شده، عامل اصلی استحکام کششی نهایی بود؛ پیکربندی این ناحیه نیز با سهم ۷/۲ درصد اثر معناداری داشت ($p < 0.001$). اثر پیکربندی به چگالی وابسته بود؛ الگوی لانه‌زنبوری صفر درجه در چگالی متوسط استحکام بیشتری ایجاد کرد، درحالی‌که الگوی خطی ±۴۵ درجه در چگالی بالا سفتی را بهبود داد. تغییرات ناگهانی بین نواحی اثر معناداری نداشت، اما گرادیان ملایم‌تر به‌صورت کیفی با حفظ بهتر استحکام همراه بود. نمونه‌های سه‌ناحیه‌ای برخلاف نمونه‌های مرجع توپر با شکست ترد، مسیرهای پیچیده انتشار ترک و رفتار شکل‌پذیر پس از تسلیم نشان دادند. بهترین طراحی، با کاهش حدود ۳۰ درصدی مصرف مواد و ۵۰ درصدی زمان چاپ، استحکام کششی را در فاصله ۵ تا ۱۳ درصدی مرجع حفظ کرد. مطلوبیت ترکیبی بهینه‌سازی چندهدفه ۰/۵۹۳ بود. نتایج، اهمیت چگالی مرکزی و ارزیابی جداگانه هندسه الگو و جهت‌گیری چاپ را در طراحی قطعات سبک تابعی‌مدرج FDM نشان می‌دهند.

کلیدواژه‌ها: مدلسازی ذوبی رسوبی، پلی‌لاکتیک اسید، پرکننده چندناحیه‌ای، بهینه‌سازی پیکربندی-چگالی، خواص کششی

نحوه ارجاع به این مقاله

نخعی امیرعلی، اکبری لالائی علی، ادیبی حامد، مهدوی آرش، بهینه‌سازی همزمان لایه‌به‌لایه چگالی و الگوی پُرشدگی در قطعات PLA چاپ‌شده به روش FDM: بررسی اثرات سلسله‌مراتبی بر رفتار کششی، مهندسی مکانیک مدرس. ۳۶۳-۳۵۱:(۰۴)۲۷؛۱۴۰۶.

*پست الکترونیکی نویسنده عهده‌دار مکاتبات: hadibi@aut.ac.ir

*شناسه ارکید نویسنده عهده‌دار مکاتبات: ۰۰۰۲-۹۹۵۶-۰۳۴۴-••••

Copyright© 2027, TMU Press. This open-access article is published under the terms of the Creative Commons Attribution-NonCommercial 4.0 International License which permits Share (copy and redistribute the material in any medium or format) and Adapt (remix, transform, and build upon the material) under the Attribution-NonCommercial terms.

1- Introduction

Additive manufacturing (AM) allows geometries that are often impossible with conventional processes, offering clear advantages in design freedom, lead time reduction, and material efficiency [1]. Among AM technologies, Fused Deposition Modeling (FDM) stands out for its low cost, accessibility, and widespread industrial use [2–5]. In FDM, a thermoplastic filament is extruded through a heated nozzle and deposited layer by layer to build a part from a digital model [6]. The resulting internal mesostructure consists of perimeters, skins, and infill. Infill has a strong influence on mechanical performance as well as on material use and print time. Simultaneously optimizing strength, material consumption, and printing time remains a practical challenge. Although FDM offers considerable design freedom, most optimization strategies apply uniform parameters across the entire part, leaving the potential of layer-wise co-optimization largely unexplored.

The layer-by-layer process gives access to parameters such as layer thickness, print speed, extrusion temperature, infill density, and infill pattern, which together govern stiffness, tensile strength, and build cost in terms of material and time [7–12]. This introduces an inherent trade-off: sparse infill saves mass and print time but creates voids that can trigger early failure [13], while near-solid infill raises mechanical strength at the cost of substantially higher material consumption and longer printing [14]. Addressing this dilemma has motivated interior designs that adapt infill locally instead of applying a uniform fill. Building on that direction, the present work systematically explores a segmented multi-zone strategy in which density and pattern are co-assigned through the thickness to quantify the contribution of each layer.

Previous investigations have established the importance of infill density, pattern geometry, and deposition orientation for the mechanical response of FDM-printed polymers. Mensah et al. [15] observed increases in the tensile strength and ductility of PLA specimens with increasing infill density. Moradi et al. [16] examined the relationships among infill percentage, layer width, and mechanical performance using response surface methodology. Dave et al. [17] investigated infill pattern and density at different part orientations, demonstrating that these variables influence tensile strength and failure behavior. Khosravani et al. [18] separately examined raster orientation and printing speed, emphasizing the importance of deposition conditions when interpreting tensile properties. Beyond nominal density, Birosz and Andó [19] investigated infill pattern scaling as a means of reducing printing time while evaluating tensile stiffness at a prescribed infill ratio. These studies show that material fraction alone does not fully describe the mechanical and manufacturing consequences of an infill design.

Recent research has extended these investigations through statistical modeling and multiobjective optimization. Rajhi et al. [20] used response surface methodology to investigate raster angle, infill percentage, and extrusion temperature in thermoplastic polyurethane, considering mechanical responses alongside part weight and build time. Malekshahi Beiranvand et al. [21] examined layer thickness, infill percentage, and raster angle in carbon-fiber-reinforced nylon, relating these parameters to fracture load, elongation, mass, and printing time. Du et al. [22] combined response surface methodology and artificial neural networks to model the tensile responses of PLA–bronze composites and subsequently performed multiobjective optimization. These studies provide useful approaches for evaluating competing responses and reporting predictive models. However, their materials, input variables, and response definitions differ, making their optimal settings specific to the investigated systems. They also address a different design question from the allocation of selected infill configurations and densities among distinct regions of a PLA component.

Spatially heterogeneous infill provides an additional means of tailoring printed structures. Sajjad et al. [23] combined different patterns within a single build and reported favorable strength-to-weight and manufacturing-efficiency outcomes for a rectangular–triangular combination relative to selected uniform-pattern specimens. Adibi et al. [24] demonstrated that the relative performance of honeycomb and auxetic sandwich cores depends on the loading mode, highlighting the need to evaluate cellular architectures against specific mechanical requirements. More directly, Hussain et al. [25] investigated functionally graded PETG specimens incorporating different infill densities and patterns through the thickness and compared their mechanical performance with uniform specimens. Such findings establish the feasibility of heterogeneous and graded architectures. They also motivate further comparisons that examine how zone-specific design choices affect mechanical performance and manufacturing efficiency under consistent material and processing conditions. Building on these developments, the present study examines the allocation of infill density and configuration among three discrete through-thickness zones in PLA tensile specimens. Each zone comprises multiple deposited layers and is assigned a nominal infill density of 30%, 60%, or 90%. Configuration is defined as a predefined pattern–orientation combination: honeycomb with a nominal 0° pattern orientation or rectilinear with alternating ±45° rasters. Treating these combinations as a single factor focuses the comparison on complete infill layouts and limits the experimental variables to configuration and density in each zone. Accordingly, differences between configurations represent their combined geometric and orientation characteristics; the separate effects of pattern geometry and raster angle cannot be identified from this design. The specific contribution is a comparative assessment of these zone-level assignments together with their mechanical and manufacturing trade-offs.

Eighteen three-zone layouts are evaluated through tensile testing, mass and printing-time measurements, and examination of fracture morphology. Statistical analysis is used to assess associations between the zone-level factors and ultimate tensile strength and elastic modulus. Fracture observations provide complementary evidence for interpreting differences among the tested layouts, while uniform reference specimens provide a basis for assessing material and time efficiency. Multiobjective optimization is then used to examine the compromise between mechanical performance and manufacturing demands. This approach provides experimental information for selecting among the investigated PLA architectures and can inform the preliminary design of lightweight fixtures, equipment enclosures, and robotic components, subject to application-specific loading and environmental requirements.

2- Materials and Methods

2-1- Overview

This study combined specimen design, fused deposition modeling, tensile testing, fracture examination, and statistical analysis to evaluate three-zone PLA structures. Tensile specimens were divided into three through-thickness zones, each assigned a nominal infill density and a predefined configuration combining pattern geometry and raster orientation. Eighteen three-zone layouts were investigated, with three specimens fabricated for each experimental condition. Printing parameters other than the investigated infill settings were held constant. Ultimate tensile strength and elastic modulus were determined from uniaxial tensile tests, while specimen mass and printing time were recorded to evaluate material use and manufacturing efficiency. Uniform-infill reference specimens were included for comparison. Descriptive statistics and signal-to-noise ratios summarized the experimental responses, and statistical modeling was used to assess associations between the zone-level factors and measured performance. Fracture observations supported the interpretation of tensile behavior. Multiobjective optimization was subsequently used to examine trade-offs between mechanical performance, mass, and printing time.

2-2- Specimen Design

Tensile specimens with a total thickness of 6 mm were designed using a geometry based on ISO 527-2:2012 (Fig. 1a) [26]. The thickness was divided into three equal zones of 2 mm each: outer zone 1 (C1), the central core zone (C2), and outer zone 2 (C3), as illustrated in Fig. 1b. Each zone comprised multiple deposited layers. The labels C1–C3 therefore identify regions within the specimen rather than individual printing layers.

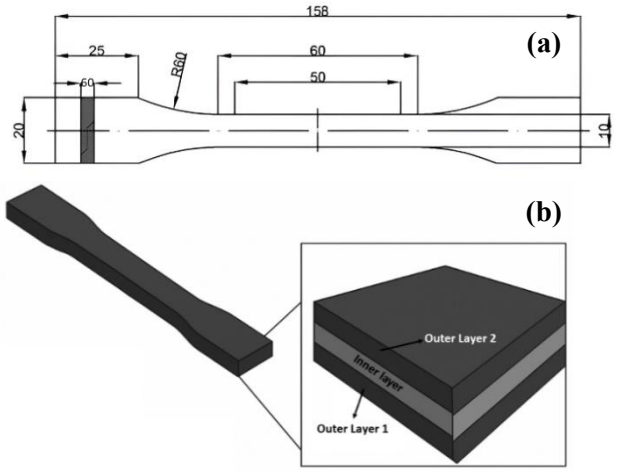


Fig. 1 a) Specimen design for tensile test according to ISO-527-2-2012 [26] b) segmentation strategy

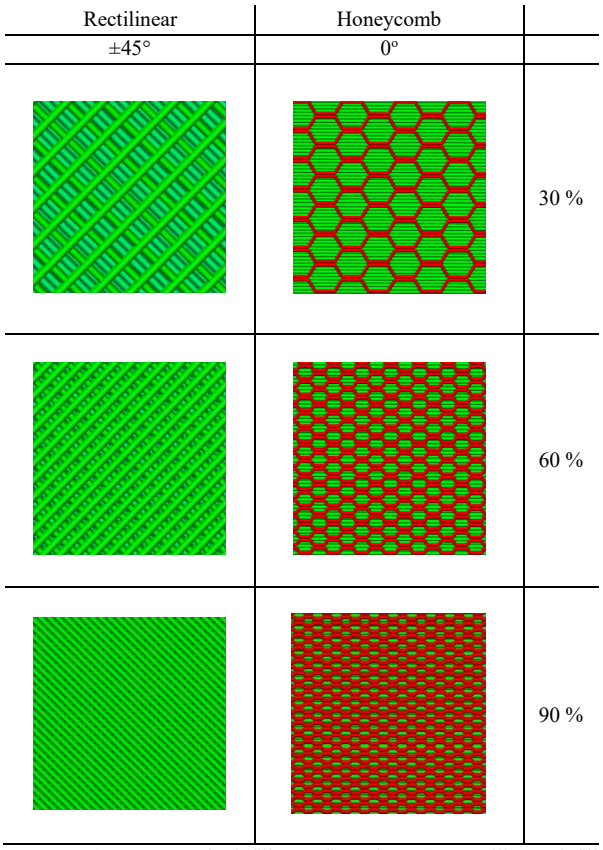


Fig. 2 A) Honeycomb infill Configuration B) Rectilinear infill Configuration

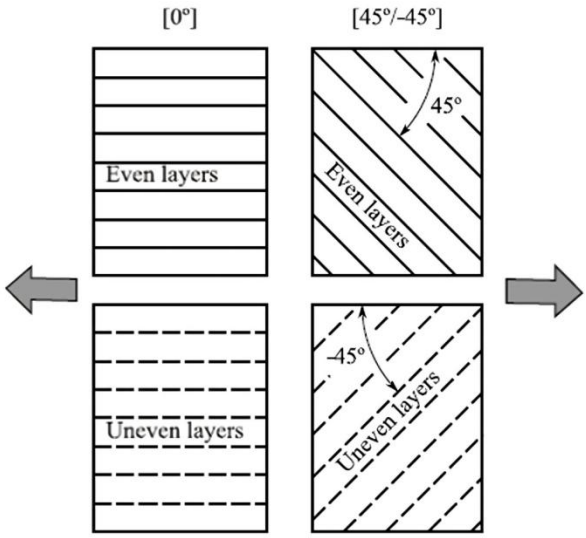


Fig. 3 comparing raster orientation 0° & 45° [27]

Each zone was assigned a nominal infill density of 30%, 60%, or 90% and one of two predefined infill configurations. These configurations were honeycomb with a nominal 0° pattern orientation and rectilinear with alternating ±45° rasters (Figs. 2 and 3). The density percentages represent the prescribed infill settings. Configuration denotes the combination of pattern geometry and its assigned deposition orientation. The experimental design focused on distributing these predefined configurations and densities among the three zones, with orientation retained as part of each configuration. Consequently, the comparison concerns complete pattern–orientation combinations, and the separate effects of geometry and raster orientation cannot be determined from this design.

External specimen dimensions and zone thicknesses were kept constant across layouts. This provided a consistent geometric basis for comparing the infill assignments in terms of tensile stiffness, ultimate tensile strength, mass, printing time, and fracture morphology.

2-3- Experimental Design

Six zone-specific experimental factors were investigated: infill configuration and nominal infill density in each of the three specimen zones (C1, C2, and C3). For each zone, the configuration factor had two levels: honeycomb with a nominal 0° pattern orientation and rectilinear with alternating ±45° raster orientations. The density factor had three levels: 30%, 60%, and 90%. The zones represent fixed geometric regions within the specimen: C1 is the first outer zone, C2 is the central core, and C3 is the second outer zone. They are not additional experimental factors or statistical blocking variables. Table 1 summarizes the six factors and their corresponding levels.

The complete factorial design space comprised 216 possible layouts, calculated as $2^3 \times 3^3$, considering three two-level configuration factors and three three-level density factors. To reduce the number of fabrication and testing conditions while screening the effects of the zone-specific parameters, an 18-run Taguchi L18-based experimental matrix was employed. The selected 18 layouts represent a reduced subset of the full factorial design; the purpose was to investigate the principal effects of the selected factors rather than to exhaustively evaluate all possible combinations or interactions.

The mixed-level structure of the L18 array does not provide mutually orthogonal columns for all three two-level configuration factors together with the three three-level density factors. Consequently, the implemented six-factor design should not be interpreted as a fully orthogonal arrangement, and some factor effects may be correlated or aliased. The actual configuration and density values assigned to each zone in every experimental run are reported in Table 2 to make the experimental arrangements explicit and reproducible. The statistical

analysis therefore focused on the six main effects, and the results were interpreted in consideration of the limitations of the reduced experimental design.

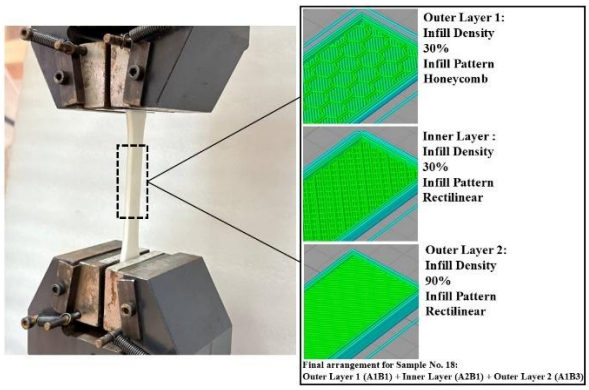


Fig. 4 Final arrangement of prepared sample in uniaxial tensile testing

Table 1 List of FDM processing parameters and their levels considered.

Factor (Symbol)	Zone	Parameter	Experimental levels	Unit
Conf_C1	C1 (Outer zone 1)	Infill configuration	Honeycomb (0°); Rectilinear (±45°)	–
Dens_C1	C1 (Outer zone 1)	Infill density	30, 60, 90	%
Conf_C2	C2 (Central core)	Infill configuration	Honeycomb (0°); Rectilinear (±45°)	–
Dens_C2	C2 (Central core)	Infill density	30, 60, 90	%
Conf_C3	C3 (Outer zone 2)	Infill configuration	Honeycomb (0°); Rectilinear (±45°)	–
Dens_C3	C3 (Outer zone 2)	Infill density	30, 60, 90	%

Note: Conf denotes infill configuration and Dens denotes nominal infill density. Honeycomb combines the honeycomb pattern with a nominal 0° orientation, whereas rectilinear combines the rectilinear pattern with alternating ±45° raster orientations. C1, C2, and C3 denote the first outer zone, central core, and second outer zone, respectively. Each zone has a fixed thickness of 2 mm.

Table 2 L18-based experimental matrix

sample Number	outer layer 1 Density	outer layer 1 pattern	inner layer Density	inner layer pattern	outer layer 2 Density	outer layer 2 pattern
1	90.00%	Rectilinear	30.00%	Rectilinear	30.00%	**Rectilinear**
2	90.00%	Rectilinear	90.00%	Rectilinear	30.00%	**Rectilinear**
3	30.00%	Rectilinear	90.00%	Rectilinear	30.00%	**Honeycomb**
4	60.00%	Rectilinear	90.00%	Rectilinear	30.00%	**Rectilinear**
5	30.00%	Honeycomb	90.00%	Honeycomb	30.00%	**Rectilinear**
6	30.00%	Rectilinear	30.00%	Honeycomb	30.00%	**Rectilinear**
7	90.00%	Rectilinear	30.00%	Honeycomb	90.00%	**Honeycomb**
8	90.00%	Honeycomb	30.00%	Honeycomb	60.00%	**Honeycomb**
9	90.00%	Rectilinear	60.00%	Rectilinear	60.00%	**Honeycomb**
10	30.00%	Rectilinear	90.00%	Rectilinear	60.00%	**Honeycomb**
11	60.00%	Rectilinear	90.00%	Honeycomb	60.00%	**Rectilinear**
12	30.00%	Honeycomb	90.00%	Rectilinear	60.00%	**Honeycomb**
13	90.00%	Rectilinear	60.00%	Honeycomb	60.00%	**Rectilinear**
14	30.00%	Honeycomb	60.00%	Honeycomb	90.00%	**Rectilinear**
15	60.00%	Honeycomb	90.00%	Rectilinear	90.00%	**Honeycomb**
16	60.00%	Rectilinear	90.00%	Rectilinear	90.00%	**Honeycomb**
17	60.00%	Rectilinear	60.00%	Rectilinear	90.00%	**Rectilinear**
18	30.00%	Honeycomb	30.00%	Rectilinear	90.00%	**Honeycomb**

2-4- Specimen Manufacturing and 3D Printing Parameters

All specimens (Fig. 5a) were fabricated from 1.75 mm eSUN PLA filament on an Ultimaker 2+ printer (Fig. 5b). Parts were printed flat on the build plate (XY plane) with layers stacked in the Z direction. G code was generated using Simplify 3D (version 4.0.1). The extruder was held at 205 °C and the heated bed at 65 °C. A 0.4 mm nozzle produced a constant layer height of 0.2 mm. The selection of the experimental parameters was guided by the previous study of Sajjad et al. [23], which investigated multiple infill strategies within a single FDM-printed part and evaluated their effects on tensile performance, material consumption, and printing time. Referring to this study provided a relevant basis for selecting the experimental conditions and establishing a comparative framework for assessing the performance of heterogeneous infill structures. The present work extends this approach by distributing infill configurations and densities across three distinct through-thickness zones. For the infill density factor, three levels (30%, 60%, and 90%) were selected to represent low, intermediate, and high-density conditions, respectively. The 30% level was chosen to provide a relatively low-density structure without introducing an extremely sparse infill condition, while 90% represents a high-density structure without reaching the fully dense (100%) condition. The intermediate level of 60% was included to provide a reference between these two conditions. This selection enables the effects of density variation on mechanical performance and manufacturing efficiency to be investigated over a broad and practically relevant range while retaining a cellular internal architecture at all levels. All fixed printing parameters are collected in Table 3; the manufacturer's filament specifications are given in Table 4.

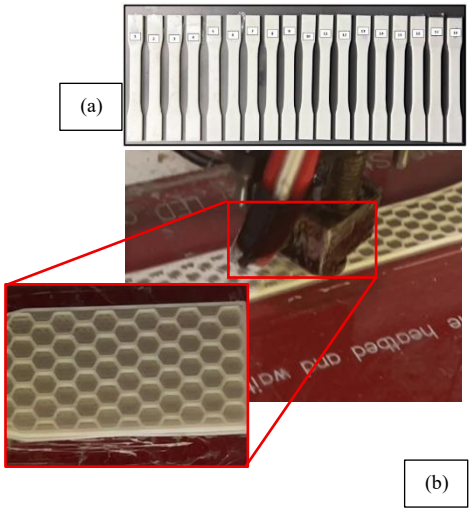


Fig. 5 a) Batch Printed Samples b) Samples Printing Process

Table 3 Constant parameters during printing [23, 28, 29]

Extruder	Diameter of nozzle	0.4 mm
	Retraction-distance	1.0 mm
	Extruder-width	0.4 mm
	Retraction-speed	1800 mm/min
Layer	Height of layer	0.2 mm
	Solid layers (top & bottom)	3
	Perimeter/outline shells	2
Temperature	Temperature of extruder	205 °C
	Temperature of heated bed	65 °C
Cooling fan	Layer-1	0
	Layer-2	100
Printing speed	Printing speed (default)	3600 mm/min

Table 4 Specification of PLA filament [30]

Parameter	Units	Recommended Value
Density at 21.5 °C	g/cm³	**1.23**
Tensile Strength	MPa	**63**
Elongation at Break	%	**20**
Filament Diameter	mm	**1.75**
Printing Temperature	°C	**195-235**
Bed Temperature	°C	**45-65**
Impact Strength	KJ/m²	**9**

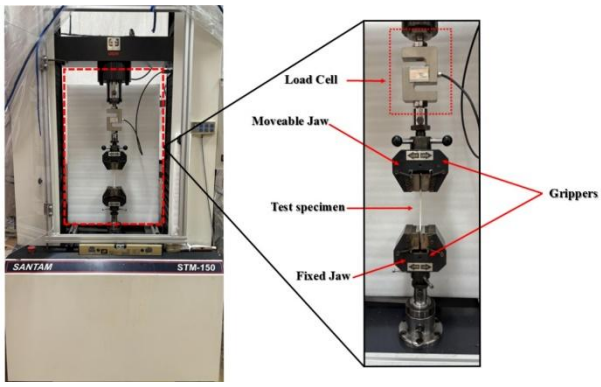


Fig. 6 STM-150 SANTAM tensile testing setup

2-5- Mechanical Testing

Uniaxial tensile tests were carried out according to ISO 527 2:2012 on a SANTAM STM 150 universal testing machine equipped with a 20 kN load cell (Fig. 6). Specimens were clamped in manual grips and pulled at a constant crosshead speed of 1 mm/min until fracture. All tests were performed at laboratory conditions of 23 ± 2 °C.

2-6- Data Collection and Statistical Analysis

Four responses were recorded for each specimen: weight, printing time, ultimate tensile strength (UTS), and elastic modulus (EM). Weight was measured on an A&D GF 3000 balance (0.01 g precision) and printing time was taken directly from the Ultimaker 2+ control software. UTS and EM were extracted from the tensile stress–strain data. Means and standard deviations were computed from the triplicate prints of each experimental run.

Taguchi signal to noise (S/N) ratios were calculated using the larger is better characteristic for UTS and EM [31-34]:

$$SN_i = -10Log[\frac{1}{n}\sum_{i=1}^{n}\frac{1}{y_i^2}] \quad (1)$$

where n is the number of replicates and yi is the measured response for the i-th replicate [35]. S/N ratios were used for descriptive ranking of factor effects. For inferential testing, a General Linear Model with Type III sums of squares was applied to the raw individual specimen data (n = 54 per response). This method was chosen because the L18 array cannot accommodate three 2 level factors in orthogonal columns without aliasing, and the GLM does not require orthogonal factor columns. Statistical significance was evaluated at α = 0.05. Descriptive statistics are reported as mean ± SD.

2-7- Quality control and benchmarks

Before testing, all specimens were visually inspected for visible defects such as under extrusion, layer misalignment, or delamination. Triplicates for each run were produced from a single PLA batch in a controlled laboratory environment (23 ± 2 °C) to limit variability arising from filament inconsistencies and ambient fluctuations.

The two fully dense reference specimens, one all rectilinear and one all honeycomb, served as uniform infill benchmarks for ultimate tensile strength, elastic modulus, mass, and print time under identical fabrication conditions.

2-8- Optical Microscopy of Fracture Surfaces

Optical microscopy of the fracture surfaces was performed using an optical microscope supplied by Faraz Teb Tajhiz (Iran). The microscope was equipped with a BEL illumination system (BEL Engineering, Italy), featuring a 21 V, 150 W lamp and an electrical rating of 230 V AC, 50 Hz. The illumination unit is marked with the designation 89/336. The observations aimed to provide qualitative information about the fracture characteristics and failure features, supporting the interpretation of the mechanical behavior of specimens fabricated with different infill densities and configurations. The optical microscopy setup used for image acquisition is shown in Fig. 7.

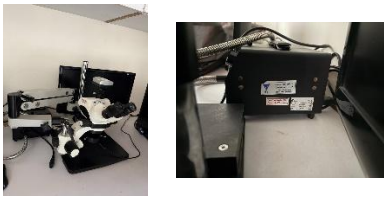


Fig. 7 Optical microscope setup used for the qualitative examination of fracture morphology in the 3D-printed PLA specimens.

3- Results and Discussion

Tensile testing of the eighteen three zone configurations (three replicates each; n = 54) revealed substantial variation in mechanical performance and mass, driven by the programmed differences in infill configuration and density across layers. Ultimate tensile strength (UTS) ranged from 25.35 ± 0.53 MPa (Sample 18) to 41.87 ± 0.84 MPa (Sample 15). Elastic modulus (EM) spanned 406.04 ± 10.72 MPa (Sample 6) to 555.21 ± 4.42 MPa (Sample 1). Specimen mass varied from 7.670 ± 0.045 g (Sample 6) to 10.330 ± 0.097 g (Sample 15), consistent with the assigned density levels (Table 2).

Experimental variability was low across all segmented conditions, indicating good repeatability of both fabrication and testing. Standard deviations for UTS ranged from 0.53 to 1.84 MPa; those for EM and mass were 4.38–10.72 MPa and 0.045–0.097 g, respectively (Table 5). The consistency among triplicates supports the statistical reliability of the observed relationships among infill density, configuration, and zone-wise layout. To quantify these effects, a General Linear Model with Type III sums of squares was applied, with the results presented below.

A clear density dependent trend emerged across the segmented specimens: increasing the core (C2) infill from 30% to 90% produced consistent gains in mechanical performance. Specimens with 90% cores (Samples 2, 3, 4, 5, 10, 11, 12, 15, 16) averaged a UTS of 35.84 ± 3.16 MPa and an EM of 495.27 ± 38.40 MPa. Those with 60% cores (Samples 9, 13, 14, 17) yielded a mean UTS of 32.11 ± 2.47 MPa and an EM of 447.45 ± 41.12 MPa, while 30% cores (Samples 1, 6, 7, 8, 18) averaged 29.54 ± 4.33 MPa in UTS and 472.61 ± 58.19 MPa in EM. Specimen mass increased from 8.30 ± 0.61 g at 30% core infill to 9.56 ± 0.50 g at 90%, with 60% cores falling at 9.28 ± 0.44 g, confirming that core infill directly governs material usage. The stress–strain curves (Fig. 8) reflected these trends: high density cores showed steeper initial slopes (ε ≈ 0–0.015) and peak stresses of 35–40 MPa near ε ≈ 0.04–0.06, whereas low density cores exhibited gentler slopes and peak values that did not exceed 27 MPa

Table 5 L18 orthogonal Array, experimental results and their S/N ratios

Sample No.	Configuration/Density (C1, C2, C3)	UTS (MPa) ± SD	EM (MPa) ± SD	Weight (g) ± SD	Time (min) ± SD
1	R / 90%, R / 30%, R / 30%	27.56 ± 0.53	555.21 ± 4.42	7.808 ± 0.069	41 ± 0.22
2	R / 90%, R / 90%, R / 30%	36.54 ± 0.88	550.11 ± 6.61	9.527 ± 0.097	44 ± 0.36
3	R / 30%, R / 90%, H / 30%	33.32 ± 0.62	490.63 ± 4.35	8.947 ± 0.069	43 ± 0.23
4	R / 60%, R / 90%, R / 30%	32.62 ± 0.70	448.94 ± 5.04	9.227 ± 0.083	43 ± 0.27
5	H / 30%, H / 90%, R / 30%	34.42 ± 0.64	450.93 ± 4.38	8.961 ± 0.069	44 ± 0.23
6	R / 30%, H / 30%, R / 30%	25.82 ± 1.84	406.04 ± 10.72	7.670 ± 0.045	41 ± 0.17
7	R / 90%, H / 30%, H / 90%	34.87 ± 0.84	516.50 ± 6.17	9.147 ± 0.097	44 ± 0.36
8	H / 90%, H / 30%, H / 60%	32.11 ± 0.70	473.56 ± 5.36	8.632 ± 0.083	43 ± 0.27
9	R / 90%, R / 60%, H / 60%	32.06 ± 0.76	408.29 ± 5.72	9.119 ± 0.097	43 ± 0.36
10	R / 30%, R / 90%, H / 60%	32.47 ± 0.70	451.58 ± 5.04	9.453 ± 0.083	44 ± 0.27
11	R / 60%, H / 90%, R / 60%	37.27 ± 0.84	538.67 ± 6.17	9.972 ± 0.097	45 ± 0.36
12	H / 30%, R / 90%, H / 60%	35.11 ± 0.70	474.25 ± 5.04	9.430 ± 0.083	44 ± 0.27
13	R / 90%, H / 60%, R / 60%	34.83 ± 0.84	469.11 ± 6.17	9.577 ± 0.097	45 ± 0.36
14	H / 30%, H / 60%, R / 90%	28.83 ± 0.70	412.38 ± 5.36	8.734 ± 0.083	45 ± 0.27
15	H / 60%, R / 90%, H / 90%	41.87 ± 0.84	544.18 ± 6.17	10.330 ± 0.097	43 ± 0.36
16	R / 60%, R / 90%, H / 90%	38.92 ± 0.84	510.09 ± 6.17	10.185 ± 0.097	45 ± 0.36
17	R / 60%, R / 60%, R / 90%	32.70 ± 0.70	502.03 ± 5.04	9.678 ± 0.083	44 ± 0.27
18	H / 30%, R / 30%, H / 90%	25.35 ± 0.53	413.74 ± 4.42	8.222 ± 0.069	41 ± 0.22

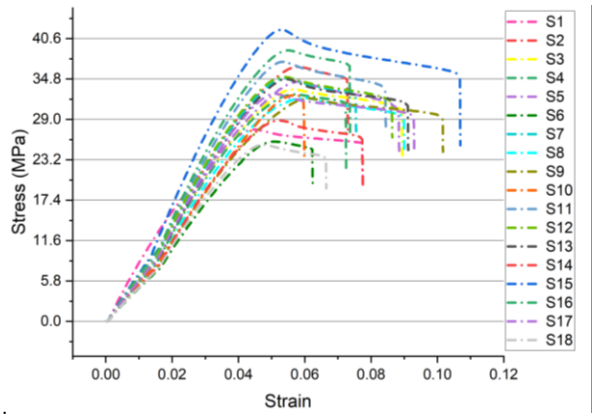


Fig. 8 Stress–strain curves for all 18 three-layer specimens

A comparative looks at moderately reinforced and uniformly low-density configurations further highlighted the influence of core infill. Sample 17, built fully rectilinear with moderate C1 and C2 densities (60%) and a denser outer shell (C3 = 90%), delivered balanced properties (UTS = 32.70 ± 0.70 MPa; EM = 502.03 ± 5.04 MPa) at a mass of 9.678 ± 0.083 g. In contrast, Sample 18, with a low-density core (C2 = 30%) and mixed honeycomb–rectilinear interfaces, recorded the lowest performance (UTS = 25.35 ± 0.53 MPa; EM = 413.74 ± 4.42 MPa; mass = 8.222 ± 0.069 g). These cases show that even modest increases in core density yield substantial gains in strength and stiffness, while uniformly low-density cores, even when paired with denser outer layers, provide limited load carrying capacity.

This reaffirms the primary role of the core layer in load transfer under tension. Statistical analysis with the General Linear Model (Type III SS) confirmed a clear hierarchy among the design parameters for UTS (Table 7). Inner layer Density (Dens_C2) was the dominant factor, accounting for 54.7 % of the explained variation ($F = 111.64$, $p < 0.001$). Outer layer 1 Density (Dens_C1) was the second largest contributor (31.2 %, $p < 0.001$). Notably, Inner layer Configuration (Conf_C2) emerged as a significant third factor (7.2 %, $p < 0.001$), a role that the standard orthogonal ANOVA had strongly understated. Outer layer 2 Density (Dens_C3) and Outer layer 2 configuration (Conf_C3) also reached significance ($p \leq 0.004$) but with smaller contributions (4.2 % and 2.3 %, respectively), while Inner layer Configuration (Conf_C1) was not significant ($p = 0.207$). Specimens with 90 % cores averaged 35.84 MPa in UTS, a 21 % increase over the 29.54 MPa recorded for 30 % cores (Fig. 9). These results confirm that the core acts as the primary load bearing region, and that the choice of infill configuration in the core exerts a genuine, non-negligible effect on tensile strength.

The main effects plot (Fig. 10) showed a sharp increase in UTS when C1 density rose from 30 % to 60 %, followed by a plateau from 60 % to 90 %, indicating diminishing returns from further densification of the inner layer. The outermost layer (C3) density contributed 4.2 %, confirming that the outer shell provides little additional strength unless the core (C2) and adjacent inner layer (C1) already carry sufficient load. Together, these results point to a load bearing hierarchy in which the core and its immediate neighbor dominate tensile resistance, while the far surface plays a secondary role.

Table 6 Response Table for Signal-to-Noise Ratios (UTS)

Level	Outer layer 1 Configuration	Outer layer 1 Density	Inner layer Configuration	Inner layer Density	Outer layer 2 Configuration	Outer layer 2 Density
1	30.25	29.69	30.20	29.22	30.56	29.96
2	30.38	31.25	30.42	30.11	30.12	30.61
3	-	30.33	-	31.06	-	30.44
Delta	0.13	1.55	0.22	1.84	0.44	0.65
Rank	6	2	5	1	4	3

Table 7 General Linear Model (Type III SS) for UTS

Source	DF	Adj SS	Adj MS	F Value	P Value	Approx. Contribution (%)
Conf_C1	1	3.27	3.27	1.64	0.207	0.4
Dens_C1	2	253.85	126.92	63.75	<0.001	31.2
Conf_C2	1	58.72	58.72	29.49	<0.001	7.2
Dens_C2	2	444.55	222.28	111.64	<0.001	54.7
Conf_C3	1	18.34	18.34	9.21	0.004	2.3
Dens_C3	2	34.03	17.01	8.54	0.001	4.2
Error	44	87.61	1.99	–	–	–
Lack of Fit	8	78.93	9.87	40.95	<0.001	–
Pure Error	36	8.68	0.24	–	–	–
Total	53	969.25	–	–	–	–

*Approx. Contribution is computed as (Adj SS of the factor / Sum of Adj SS of all six factors) × 100. The sum of these six values is 100 % because error variation is excluded.

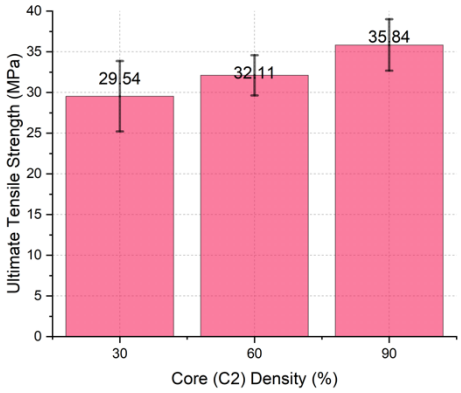


Fig. 9 Effect of inner core (C2) infill density on ultimate tensile strength (UTS) in segmented FDM samples.

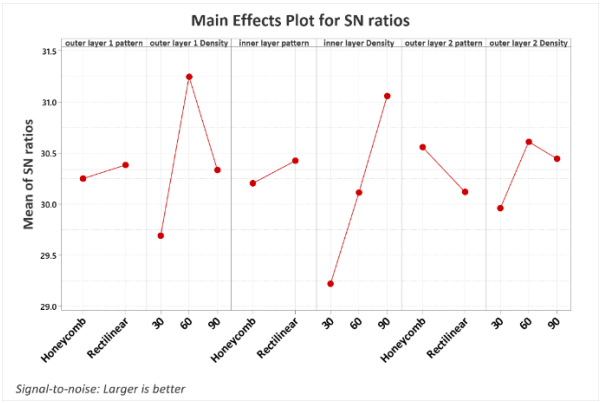


Fig. 10 Main Effects Plot for SN ratio of UTS

Analysis of elastic modulus with the General Linear Model (Table 8) showed that stiffness is governed primarily by density, with Inner Layer Density (Dens_C2) contributing 64.34 % of the explained variation ($F = 72.91$, $p < 0.001$). Outer layer 1 Density (Dens_C1, 19.44 %) and Outer layer 2 Density (Dens_C3, 12.51 %) were also significant ($p < 0.001$). Among the configuration factors, only Inner Layer configuration (Conf_C2) had a reliable effect (3.61 %, $p = 0.006$); Outer layer 1 and 2 configuration were not significant ($p > 0.6$). The main effects plot (Fig. 11) and S/N descriptive ranking (Table 9) placed Outer layer 1 Density (Dens_C1) first in raw magnitude ($\Delta = 1.21$), with a nonlinear trend peaking at 60 % density, while Inner Layer Density (Dens_C2) ($\Delta = 0.88$). This difference between the S/N ranking and the GLM contribution order reflects the non-orthogonal design. The lack of fit was significant ($p < 0.001$), and the residual standard error remained relatively high ($S = 27.50$ MPa), indicating that the six-factor main-effects model did not fully capture the observed variation in elastic modulus. This limitation may be associated with unmodeled interactions among zone-specific factors, nonlinear response behavior, or other sources of variation not included in the model. However, since interaction terms were not explicitly incorporated into the GLM, their presence and statistical significance cannot be confirmed from the present analysis.

Differences in tensile response were observed among specimens with different zone-wise density distributions and configurations (Fig. 12).

Table 8 General Linear Model (Type III SS) for Elastic Modulus

Source	DF	Adj SS	Adj MS	F Value	P Value	Approx. Contribution (%)
Conf_C1	1	162	162	0.21	0.646	0.1
Dens_C1	2	33328	16664	22.03	<0.001	19.4
Conf_C2	1	6186	6186	8.18	0.006	3.6
Dens_C2	2	110283	55141	72.91	<0.001	64.3
Conf_C3	1	4	4	0.01	0.939	<0.1
Dens_C3	2	21448	10724	14.18	<0.001	12.5
Error	44	33276	756	–	–	–
Lack of Fit	8	30420	3802	47.93	<0.001	–
Pure Error	36	2856	79	–	–	–
Total	53	241357	–	–	–	–

*Approx. Contribution = (Adj SS of factor / Sum of Adj SS of all six factors) × 100

Table 9 Response Table for Signal to Noise Ratios (EM)

Level	Outer layer 1 Configuration	Outer layer 1 Density	Inner layer Configuration	Inner layer Density	Outer layer 2 Configuration	Outer layer 2 Density
1	53.24	52.90	53.34	53.43	53.51	53.64
2	53.71	54.11	53.69	52.99	53.60	53.40
3	-	53.85	-	53.87	-	53.63
Delta	0.47	1.21	0.35	0.88	0.08	0.24
Rank	3	1	4	2	6	5

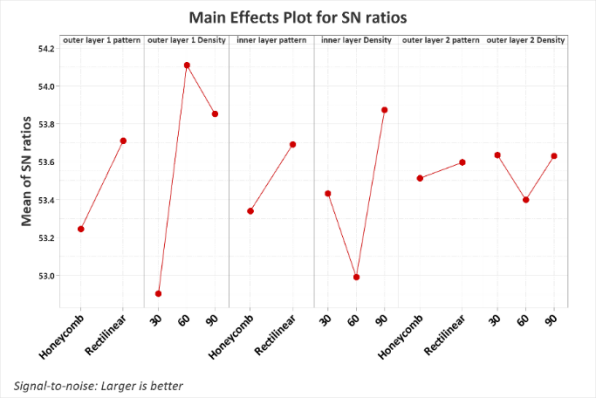


Fig. 11 Main Effects Plot for SN ratio of EM

For example, Sample 1 (R90/R30/R30) exhibited a UTS of 27.56 ± 0.53 MPa and an EM of 555.21 ± 4.42 MPa, whereas Sample 15 (H60/R90/H90) achieved a UTS of 41.87 ± 0.84 MPa and an EM of 544.18 ± 6.17 MPa. Although Sample 1 contained a larger density drop between C1 and C2 than Sample 15, these two layouts also differed in the density assigned to each zone and in their infill configurations. Therefore, their performance differences cannot be attributed to transition magnitude alone. The fracture images in Fig. 12 illustrate differences in fracture morphology; however, they do not directly measure local stress concentrations or establish that the observed density transitions caused the differences in tensile strength. The observed fracture features may be consistent with variations in local load transfer near zone boundaries, but this interpretation remains qualitative within the scope of the present experimental design.

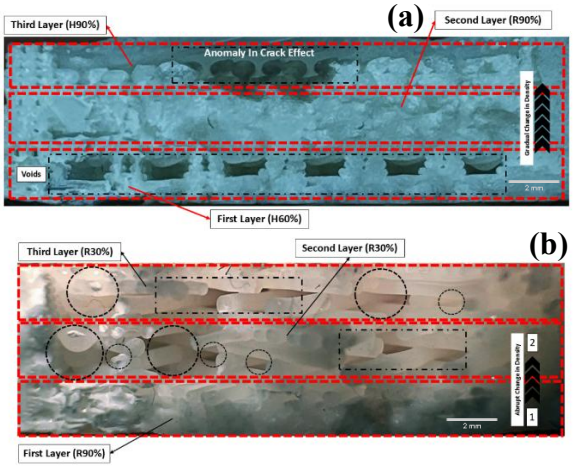


Fig. 12 Fracture morphology comparison of segmented FDM structures with (a) gradual and (b) abrupt infill density transitions.

To examine whether inter-zone transitions were related to tensile performance, two descriptive indicators were considered: the maximum absolute density difference between adjacent zones (in percentage points) and the number of configuration changes (honeycomb ↔ rectilinear). The descriptive comparison did not reveal a clear independent relationship between either indicator and UTS or EM. Although some layouts with relatively small density differences and no configuration changes exhibited higher UTS values, while some layouts combining larger density differences with configuration changes showed lower values, these patterns were not statistically established and cannot be separated from the simultaneous effects of zone-specific density and configuration. Although 54 specimens were tested, they represented 18 distinct layouts, each fabricated in triplicate. Thus, the triplicates provide information on within-layout variability but do not increase the number of distinct transition arrangements investigated. Consequently, the fracture images should be interpreted as qualitative observations of fracture morphology rather than statistical evidence that abrupt transitions cause interface-localized failure or reduce tensile strength. Within the scope of the present study, transition characteristics should therefore be regarded as a secondary factor requiring further investigation through a dedicated experimental design.

When core (inner layer) density was held constant, differences in tensile response were also observed between the selected infill configurations. At 60% core density, honeycomb (0°) produced a higher UTS, whereas at 90% core density, rectilinear (±45°) showed a small stiffness advantage (Fig. 13). These observations suggest that the relative performance of the configurations may vary with local density, although this trend should be interpreted descriptively because interaction terms were not included in the GLM.

The interaction plot (Fig. 14) further illustrates this behavior. At a C1 density of 60%, the combination of a rectilinear inner-shell configuration with a honeycomb core exhibited a stiffness peak of approximately 540 MPa, exceeding the rectilinear–rectilinear combination. This pattern may indicate that geometric compatibility between adjacent zones contributes to the elastic response. Nevertheless, it does not establish a statistically significant higher-order interaction. Such interactions may be among the factors contributing to the unexplained variation in the EM model, but their effects require further investigation through an experimental design that explicitly incorporates and tests interaction terms.

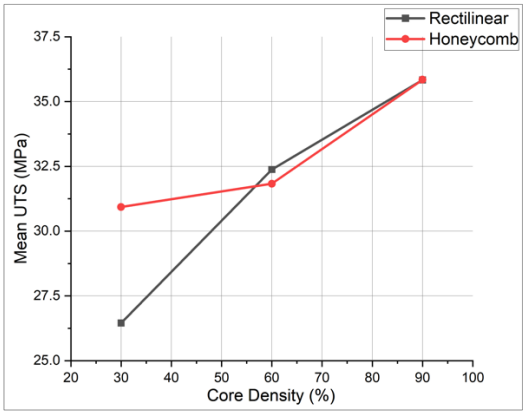


Fig. 13 Effect of core density and pattern on ultimate tensile strength (UTS) in segmented FDM structures. A crossover trend is observed

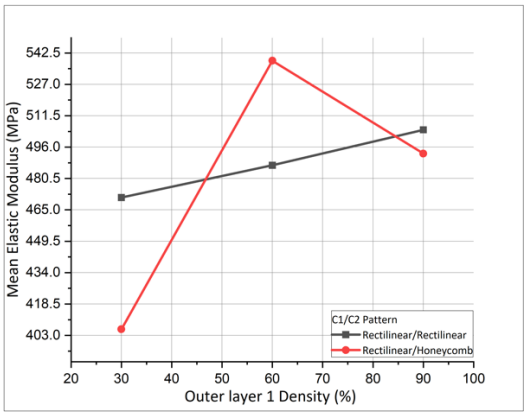


Fig. 14 Interaction between outer layer 1 (C1) density and inner layer (C2) pattern on elastic modulus.

Layer wise comparison of the S/N ratios showed that configuration effects were most visible at the outer surfaces. In the outermost zone (C3), switching from rectilinear ±45° to honeycomb 0° raised the S/N ratio by 0.44 dB, consistent with the honeycomb skin helping to distribute surface stresses and delay crack initiation. In the inner shell (C1), the two configurations gave nearly the same S/N at equal density (difference only 0.13 dB), so density clearly dominated there. In the core (C2), the S/N difference was also small ($\Delta S/N = 0.22$ dB), although the GLM confirmed that core configuration is in fact a statistically significant secondary factor.

Taken together, these results confirm that density is the main driver of tensile behavior, while the choice of configuration, particularly in the core, can fine tune strength and stiffness when matched to the local density. The density dependent tradeoffs just described fit well with the fracture surface observations discussed below.

Fracture morphology depended on the local configuration, the density level, and how sharply the infill changed from one zone to the next. Segmented specimens with a rectilinear core and honeycomb outer layers produced winding crack paths and rough fracture surfaces with multiple kinks (Fig. 15a), which points to greater energy dissipation along the crack. In contrast, the fully dense uniform benchmarks, both rectilinear and honeycomb, showed flat, stepped fracture surfaces typical of brittle, straight through fracture under tension (Fig. 15b–c).

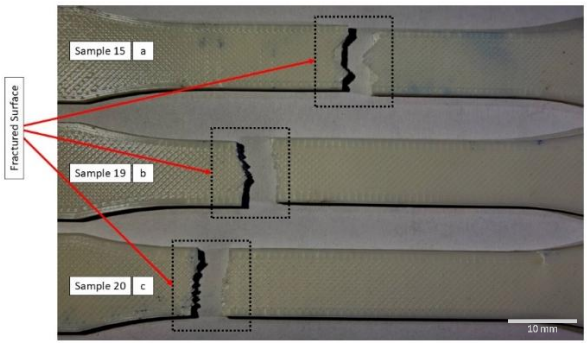


Fig. 15 Fracture surface morphology of selected FDM-printed tensile samples. (a) Sample 15 exhibits deflected and tortuous crack paths due to infill segmentation. (b) Sample 19 and (c) Sample 20 represent benchmark samples with uniform infill structures showing linear fracture surfaces.

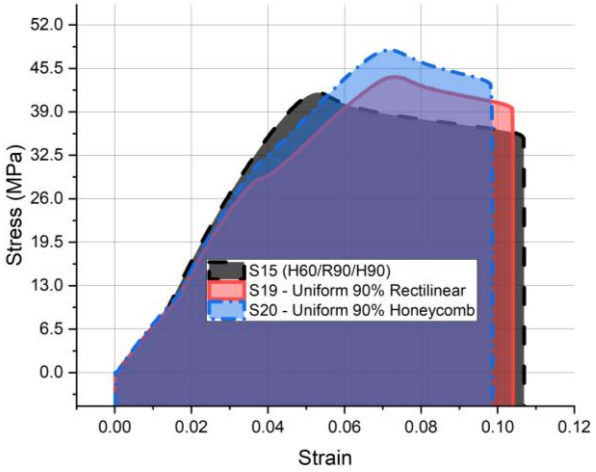


Fig. 16 Comparison between Sample 15 and two benchmarks

The stress–strain curves matched these observations (Fig. 16). Tortuous cracks gave a longer post yield tail with a gradual stress drop, indicating more ductile behavior, whereas the planar fracture planes in the uniform references caused a sudden failure with little plastic deformation. A representative segmented build (H60/R90/H90) reached a UTS of 41.87 ± 0.84 MPa, close to the uniform benchmarks (44.21 MPa for rectilinear and 48.23 MPa for honeycomb) but consumed roughly 30 % less material and about half the printing time. This shows that crack deflection can help maintain strength while noticeably improving build efficiency.

Features specific to each configuration reinforced these trends. Parts with a large honeycomb fraction displayed zigzag crack paths that went around the hexagonal cells (Fig. 17), whereas parts with a mainly rectilinear core showed stepped surfaces that followed the filament direction (Fig. 18). Dense honeycomb cores could give a higher peak strength than rectilinear ones at the same density, though it must be kept in mind that this comparison bundles cell shape and raster angle together. Rectilinear layouts, on the other hand, tended to provide slightly higher stiffness because they offer uninterrupted axial load paths during the elastic stage.

Fracture morphology also varied among specimens with different core densities and zone-wise infill arrangements. In particular, specimens with a 30% core density exhibited an open and porous internal structure (Fig. 19), while the layout illustrated in Fig. 20 displayed irregular fracture features across regions with different infill assignments.

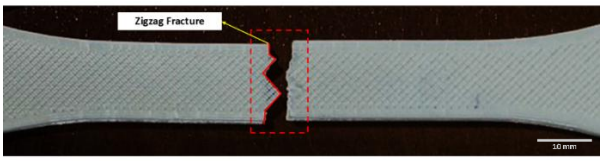


Fig. 17 Zigzag fracture surface observed in a sample with dominant honeycomb infill.

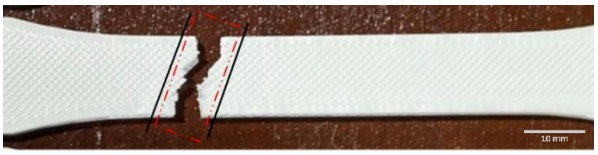


Fig. 18 Fracture surface featuring a rectilinear core enclosed by honeycomb outer layers.

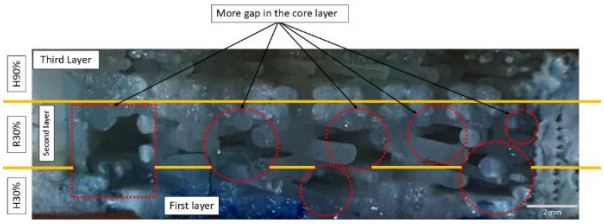


Fig. 19 Cross-sectional morphology featuring a low-density (30%) rectilinear core layer enclosed by honeycomb outer layers.

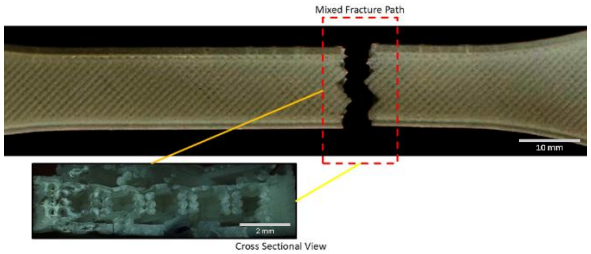


Fig. 20 Fracture surface and internal structure featuring an abrupt transition from honeycomb (30%) to honeycomb (60%) to rectilinear (90%) infill.

These morphological characteristics may reflect differences in local load-bearing area and crack propagation paths. However, local stress and strain fields were not directly measured or numerically evaluated in this study, and density and configuration varied simultaneously among the specimen zones. Therefore, the observed fracture features cannot establish that abrupt transitions directly caused stress concentrations or reductions in tensile strength. These images are presented as qualitative observations that complement the measured tensile responses and help describe the fracture behavior of the investigated multi-zone structures.

To place the segmented design in context, the best performing three zone specimen (H60/R90/H90) was compared with the two fully dense uniform benchmarks and also with the design of Sajjad et al. [23]. The uniform rectilinear benchmark reached 44.21 MPa with a mass of 14.45 g, and the uniform honeycomb benchmark reached 48.23 MPa with a mass of 14.56 g. The best performing segmented specimen achieved 41.87 MPa, which is within 5–13% of these reference strengths, while using roughly 30% less material and about 50% less printing time (Table 10). The strength to weight ratio of the segmented design (4.05 MPa/g) was approximately double that of the uniform references (3.06 MPa/g for rectilinear, 3.31 MPa/g for honeycomb). This comparison confirms that layer wise co optimization can largely close the strength gap to solid infill while delivering substantial material and time savings.

Table 10 Performance comparison: segmented design vs. uniform benchmarks and prior graded-pattern work.

Performance Metric	Uniform rectilinear (100%)	Uniform honeycomb (100%)	Segmented (H60/R90/H90)	Sajjad et al. [23]
UTS (MPa)	44.21	48.23	41.87	17.03
Mass (g)	14.45	14.56	10.33	12.09
Print time (min)	86	86	43	47
Strength-to-weight (MPa/g)	3.06	3.31	4.05	1.41

Table 11 Regression Model Summary Statistics

Response	R-sq (%)	R-sq(adj) (%)	R-sq(pred) (%)	S (Std. Dev. of Error)
Weight (g)	96.68	92.94	82.67	0.1965
Elastic Modulus (MPa)	86.21	83.39	79.77	27.50
UTS (MPa)	90.96	89.11	86.82	1.41
Printing Time (min)	91.34	81.59	56.56	0.5741

Empirical regression models were developed from the individual specimen data (n = 54) to relate the six input factors to the four responses (Table 11). Predictive accuracy was high for all responses. The models for weight (R^2 = 96.7 %) and printing time (R^2 = 91.3 %) were excellent. The UTS model achieved R^2 = 91.0 % with a predictive R^2 of 86.8 %, while the EM model gave R^2 = 86.2 % and R^2(pred) = 79.8 %.

A multi-objective optimization was performed to maximize ultimate tensile strength (UTS) and elastic modulus (EM), while minimizing specimen mass and printing time (Table 12). The optimization yielded a composite desirability of 0.593 (Table 13). In the desirability approach, this dimensionless index ranges from 0 to 1, where 1 represents the ideal simultaneous satisfaction of all response objectives, whereas 0 indicates that at least one response falls outside its specified acceptable limits. Accordingly, the obtained value of 0.593 should be interpreted as an intermediate overall desirability rather than a near-ideal solution. It does not represent a percentage of prediction accuracy or an absolute measure of optimization success.

The intermediate desirability reflects the competing requirements of the four responses: increasing infill density can improve load-bearing capacity and stiffness, but may also increase material consumption and manufacturing time. Consequently, a single configuration cannot necessarily maximize both mechanical responses while simultaneously minimizing mass and printing time. The identified solution, consisting of a 60% honeycomb C1 zone, a 90% rectilinear C2 core, and a 30% honeycomb C3 zone, represents the best overall compromise identified by the optimizer under the selected response goals and constraints. Therefore, its practical relevance should be evaluated in terms of the combined mechanical performance and manufacturing benefits, rather than the desirability value alone.

Table 12 Optimization objectives and experimentally observed response ranges

Response	Experimental maximum	Experimental minimum	Optimization objective	Unit
Ultimate tensile strength (UTS)	41.87	25.35	Maximize	**MPa**
Elastic modulus (EM)	555.21	406.04	Maximize	**MPa**
Specimen weight	10.330	7.670	Minimize	**g**
Printing time	45	41	Minimize	**min**

Table 13 Optimal Solution and Predicted Performance

Parameter	Optimal Setting	Predicted Response	Fit	Composite Desirability
Outer Layer 1 Configuration	Honeycomb	Printing Time (min)	41.70	–
Outer Layer 1 Density	60 %	Weight (g)	9.29	–
Inner Layer Configuration	Rectilinear	EM (MPa)	666.1	–
Inner Layer Density	90 %	UTS (MPa)	37.49	–
Outer Layer 2 Configuration	Honeycomb	–	–	0.593
Outer Layer 2 Density	30 %	–	–	–

4- Conclusion

A multi zone segmented infill strategy was developed and tested to improve the mechanical performance and material efficiency of FDM printed PLA parts. By independently assigning infill density and configuration (pattern plus its typical raster orientation) to three through thickness zones within a structured experimental design, the hierarchy of design parameters was resolved and the influence of inter zone transitions on tensile behavior was quantified.

Key findings:

Hierarchy of effects. Core (C2) density was the dominant factor for UTS, explaining 54.7 % of the explained variation, followed by inner shell (C1) density (31.2 %). For elastic modulus, core density was also the dominant factor among the investigated main effects (64.34%), followed by C1 density (19.44%). However, the significant lack of fit ($p < 0.001$) and the residual standard error of 27.50 MPa indicate that the main-effects model did not fully explain the observed stiffness variation. Possible contributions from unmodeled interactions among zone-specific factors, nonlinear behavior, or other unexamined variables cannot be ruled out; however, these effects were not independently tested in the present study.

Density conditioned configuration effects. Core configuration was a statistically significant factor for both UTS ($p < 0.001$) and EM ($p = 0.006$). The optimal configuration depended on the local density: honeycomb 0° gave higher strength at moderate core densities, while rectilinear ±45° offered a stiffness advantage at high core densities. Configuration should therefore be co optimized with density, not chosen independently.

Inter-zone transitions. The tested layouts exhibited qualitative differences in fracture morphology that may be related to variations in density and configuration between adjacent zones. However, the descriptive transition indicators did not establish a clear independent relationship with UTS or EM, and the present experimental design does not isolate transition effects from the individual zone-level factors. Accordingly, the results do not demonstrate that abrupt transitions necessarily reduce tensile strength or that smoother transitions necessarily improve it. The potential influence of interface design should therefore be considered a secondary research consideration requiring further investigation through dedicated experimental designs involving a larger number of distinct transition arrangements and, where possible, local stress and strain characterization.

Fractography confirmed the mechanical trends. Segmented layouts with contrasting shell and core configurations produced tortuous, deflected crack paths and extended post yield deformation, indicating ductile behavior. Uniform infill references, in contrast, failed in a brittle manner with flat fracture surfaces.

Modelling and optimization. Regression models were developed to predict mass, UTS, EM, and printing time. Multi-objective optimization yielded a composite desirability of 0.593, indicating an intermediate compromise among the four competing response objectives rather than a near-ideal solution. The selected configuration comprised a 60% honeycomb inner shell (C1), a 90% rectilinear core (C2), and a 30% honeycomb outer shell (C3). This configuration provides a balanced combination of mechanical performance and manufacturing efficiency within the investigated design space.

Benchmarking. Relative to fully dense uniform references, the optimized segmented design achieved comparable UTS (within 5–13 %) while consuming roughly 30 % less material and about 50 % less print time. Compared with earlier pattern only graded designs that kept density fixed, the segmented co optimization delivered a substantially higher strength to weight ratio, primarily because a dense core was introduced.

Implications:

The tensile performance of multi zone segmented FDM parts is governed first by the amount and distribution of load bearing material, and can be fine-tuned by matching the configuration to the local density and by keeping inter zone transitions smooth. In practice, a dense rectilinear core combined with a moderately dense honeycomb inner shell and a light honeycomb outer shell can maintain tensile strength while significantly reducing mass and print time, offering a practical route to lightweight functional components for robotics, tooling, and prototyping.

Limitations and future work:

The study was limited to PLA, two infill configurations (honeycomb 0° and rectilinear ±45°), and uniaxial tension. Because raster orientation was tied to the pattern within each configuration, the separate effects of cell geometry and raster angle could not be isolated. Future work should decouple these variables in a full factorial design and extend the investigation to other materials (ABS, PETG), additional infill geometries, varied raster angles, and other loading modes including compression, bending, impact, and fatigue. The weaker performance of the EM model highlights the need for physics informed or finite element assisted approaches, together with higher resolution characterization such as porosity mapping or micro–CT. Process parameters (nozzle temperature, print speed, layer height) and the deliberate design of gradual or curved interfaces also merit further study to refine stiffness without sacrificing efficiency.

Artificial Intelligence Statement: ChatGPT (OpenAI) was used solely for English language editing and linguistic refinement of the manuscript. The authors reviewed and verified all AI-assisted revisions and take full responsibility for the accuracy, originality, and integrity of the manuscript.

Acknowledgements: The authors would like to express their sincere gratitude to all individuals and colleagues who provided assistance, support, and valuable contributions throughout this research.

Funding: This research received no specific grant from any funding agency in the public, commercial, or not-for-profit sectors.

CRediT Authorship Contribution: The authors declare that they have no known competing financial interests or personal relationships that could have appeared to influence the work reported in this paper.

Conflict of Interest: Amirali Nakhaei: Conceptualization, Methodology, Investigation, Formal Analysis, Data Curation, and Writing – Original Draft; Ali Akbari Lalaei: Conceptualization, Methodology, Investigation, and Formal Analysis; Hamed Adibi: Supervision, Project Administration, Validation, Conceptualization, and Writing – Review & Editing; Arash Mahdavi: Investigation and Writing – Original Draft.

References

[1] M. K. Thompson et al., "Design for additive manufacturing: Trends, opportunities, considerations, and constraints," *CIRP Annals*, vol. 65, no. 2, pp. 737–760, 2016, doi: 10.1016/j.cirp.2016.05.004.

[2] I. Gibson, "Rapid prototyping: From product development to medicine and beyond," *Virtual and Physical Prototyping*, vol. 1, no. 1, pp. 31–42, 2006, doi: 10.1080/17452750500271298.

[3] A. S. Mazaheri, V. Abedini, and A. Kami, "Effects of raster angle and composition of layers on tensile and flexural properties of PLA-PLA/Al multimaterial manufactured by fused deposition modeling," *Proceedings of the Institution of Mechanical Engineers, Part E: Journal of Process Mechanical Engineering*, vol. 239, no. 1, pp. 213–220, 2025, doi: 10.1177/09544089231175202.

[4] S. M. B. Mirafzali, A. Hasanabadi, and H. Afshari, "Investigating the effect of process parameters on the tensile strength of PLA parts produced by FDM method using the response surface method," *Modares Mechanical Engineering*, vol. 22, no. 10, pp. 235–239, 2022.

[5] A. A. Elsonbaty, A. M. Rashad, O. Y. Abass, T. Y. Abdelghany, and A. M. Alfauiomy, "A survey of fused deposition modeling (FDM) technology in 3D printing," *Journal of Engineering Research and Reports*, vol. 26, no. 11, pp. 304–312, 2024, doi.: 10.9734/jerr/2024/v26i111332.

[6] A. Cano-Vicent et al., "Fused deposition modelling: Current status, methodology, applications and future prospects," *Additive Manufacturing*, vol. 47, Art. no. 102378, 2021, doi: 10.1016/j.addma.2021.102378.

[7] M. V. Ehteshamfar, M. S. Javadi, and H. Adibi, "Surface modification of prototypes in fused deposition modelling using lapping process," *Rapid Prototyping Journal*, vol. 28, no. 7, pp. 1382–1393, 2022, doi: 10.1108/RPJ-06-2021-0148.

[8] S. Patel et al., "Effect of infill pattern on the mechanical properties of PLA and ABS specimens prepared by FDM 3D printing," *Proceedings of the Institution of Mechanical Engineers, Part E: Journal of Process Mechanical Engineering*, vol. 240, no. 2, pp. 1759–1767, 2026, doi: 10.1177/09544089241258744.

[9] D. Popescu, A. Zapciu, C. Amza, F. Baciu, and R. Marinescu, "FDM process parameters influence over the mechanical properties of polymer specimens: A review," *Polymer Testing*, vol. 69, pp. 157–166, 2018, doi: 10.1016/j.polymertesting.2018.05.020.

[10] M. Kamaal, M. Anas, H. Rastogi, N. Bhardwaj, and A. Rahaman, "Effect of FDM process parameters on mechanical properties of 3D-printed carbon fibre–PLA composite," *Progress in Additive Manufacturing*, vol. 6, no. 1, pp. 63–69, 2021, doi: 10.1007/s40964-020-00145-3.

[11] J. K. Sahu, R. K. Sahu, J. K. Katiyar, and P. S. Kiran, "Optimisation of process parameters for dimensional stability in FDM," *Proceedings of the Institution of Mechanical Engineers, Part E: Journal of Process Mechanical Engineering*, first published online Oct. 17, 2023, doi: 10.1177/09544089231206800.

[12] D. Syrlybayev, B. Zharylkassyn, A. Seisekulova, M. Akhmetov, A. Perveen, and D. Talamona, "Optimisation of strength properties of FDM printed parts—A critical review," *Polymers*, vol. 13, no. 10, Art. no. 1587, 2021, doi: 10.3390/polym13101587.

[13] X. Sun, M. Mazur, and C.-T. Cheng, "A review of void reduction strategies in material extrusion-based additive manufacturing," *Additive Manufacturing*, vol. 67, Art. no. 103463, 2023, doi: 10.1016/j.addma.2023.103463.

[14] S. K. Prajapati and R. Gnanamoorthy, "Effect of the infill percentage of 3D printed Polyetheretherketone under the dry sliding condition," *Journal of Manufacturing Processes*, vol. 131, pp. 2073–2081, 2024, doi: 10.1016/j.jmapro.2024.10.035.

[15] R. A. Mensah, D. A. Edström, O. Lundberg, V. Shanmugam, L. Jiang, X. Qiang, et al., "The effect of infill density on the fire properties of polylactic acid 3D printed parts: A short communication," *Polymer Testing*, vol. 111, Art. no. 107594, 2022, doi: 10.1016/j.polymertesting.2022.107594.

[16] M. Moradi, M. Rezayat, F. A. R. Rozhbiany, S. Meiabadi, G. Casalino, M. Shamsborhan, et al., "Correlation between infill percentages, layer width, and mechanical properties in fused deposition modelling of poly-lactic acid 3D printing," *Machines*, vol. 11, no. 10, Art. no. 950, 2023, doi: 10.3390/machines11100950.

[17] H. K. Dave, N. H. Patadiya, A. R. Prajapati, and S. R. Rajpurohit, "Effect of infill pattern and infill density at varying part orientation on tensile properties of fused deposition modeling-printed poly-lactic acid part," *Proceedings of the Institution of Mechanical Engineers, Part C: Journal of Mechanical Engineering Science*, vol. 235, no. 10, pp. 1811–1827, 2021, doi: 10.1177/0954406219856383.

[18] M. R. Khosravani, F. Berto, M. R. Ayatollahi, and T. Reinicke, "Characterization of 3D-printed PLA parts with different raster orientations and printing speeds," *Scientific Reports*, vol. 12, Art. no. 1016, 2022, doi: 10.1038/s41598-022-05005-4.

[19] M. T. Birosz and M. Andó, "Effect of infill pattern scaling on mechanical properties of FDM-printed PLA specimens," *Progress in Additive Manufacturing*, vol. 9, no. 4, pp. 875–883, 2024, doi: 10.1007/s40964-023-00487-8.
[20] W. Rajhi, A. B. M. Ali, D. J. Jasim, O. Mehrabi, L. Ben Said, and M. Moradi, "Mathematical and statistical analysis of fused filament fabrication parameters for thermoplastic polyurethane parts via response surface methodology," *Mathematics*, vol. 12, no. 19, Art. no. 3146, 2024, doi: 10.3390/math12193146.
[21] Z. Malekshahi Beiranvand, H. Abdollahi, N. Salimi, O. Mehrabi, and M. Moradi, "Experimental analysis of 3D-printed carbon fiber-reinforced nylon composites manufactured by fused deposition modeling using a statistical approach," *Journal of Materials Engineering and Performance*, vol. 35, pp. 16143–16165, 2026, doi: doi: 10.1007/s11665-025-12783-1.
[22] G. Du, E. Ghanbary, O. Mehrabi, R. Barzamini, and M. Moradi, "Integrating response surface methodology and machine learning for multi-objective optimization of fused deposition modeling parameters in 3D-printed polylactic acid–bronze composites," *Polymer for Advanced Technologies*, vol. 37, no. 4, Art. no. e70587, 2026, doi: 10.1002/pat.70587.
[23] R. Sajjad, S. U. Butt, H. A. Saeed, M. T. Anwar, and T. Rasheed, "Impact of multiple infill strategy on the structural strength of single build FDM printed parts," *Journal of Manufacturing Processes*, vol. 89, pp. 105–110, 2023, doi: 10.1016/j.jmapro.2023.01.065.
[24] H. Adibi, A. Akbari Lalaei, and A. Nakhaei, "Unified experimental and finite element analysis of the mechanical performance of 3D-printed honeycomb and auxetic sandwich cores," *Composites Part C: Open Access*, vol. 18, Art. no. 100656, 2025, doi: 10.1016/j.jcomc.2025.100656.
[25] S. A. Hussain, M. S. Charoo, and M. I. U. Haq, "Mechanical performance of 3D printed functionally graded PETG: An experimental investigation," *Next Materials*, vol. 9, Art. no. 101093, 2025, doi: 10.1016/j.nxmate.2025.101093.
[26] International Organization for Standardization, *Plastics—Determination of Tensile Properties—Part 2: Test Conditions for Moulding and Extrusion Plastics*, ISO 527-2:2012, Geneva, Switzerland: ISO, 2012. (No DOI assigned.)
[27] S. Farah, D. G. Anderson, and R. Langer, "Physical and mechanical properties of PLA, and their functions in widespread applications—A comprehensive review," *Advanced Drug Delivery Reviews*, vol. 107, pp. 367–392, 2016, doi: 10.1016/j.addr.2016.06.012.
[28] R. Sajjad, S. U. Butt, K. Mahmood, and H. A. Saeed, "Investigating the impacts of heterogeneous infills on structural strength of 3D printed parts," *Key Engineering Materials*, vol. 799, pp. 276–281, 2019 doi: 10.4028/www.scientific.net/KEM.799.276.
[29] H. Safi Valilu, M. A. Saeimi Sadigh, M. Sajed, and V. Tavousi, "Experimental and numerical analysis of energy absorption in 3D-printed auxetic and combined lattice structures under quasi-static loading," *Modares Mechanical Engineering*, vol. 25, no. 9, pp. 555–565, 2025, doi: 10.48311/mme.2025.27793.
[30] E. Monaldo, M. Ricci, and S. Marfia, "Mechanical properties of 3D printed polylactic acid elements: Experimental and numerical insights," *Mechanics of Materials*, vol. 177, Art. no. 104551, 2023, doi: 10.1016/j.mechmat.2022.104551.
[31] S. Akhondi, C.-D. Matte, and T. H. Kwok, "A study on mechanical behavior of 3D printed elastomers with various infills and densities," *Manufacturing Letters*, vol. 35, suppl., pp. 592–602, 2023, doi: 10.1016/j.mfglet.2023.08.035.
[32] M. Heidari-Rarani, N. Ezati, P. Sadeghi, and M. R. Badrossamay, "Optimization of FDM process parameters for tensile properties of polylactic acid specimens using Taguchi design of experiment method," *Journal of Thermoplastic Composite Materials*, vol. 35, no. 12, pp. 2435–2452, 2022, doi: 10.1177/0892705720964560.
[33] B. A. Ahmed, U. Nadeem, A. S. Hakeem, A. Ul-Hamid, M. Y. Khan, M. Younas, et al., "Printing parameter optimization of additive manufactured PLA using Taguchi design of experiment," *Polymers*, vol. 15, no. 22, Art. no. 4370, 2023, doi: 10.3390/polym15224370.
[34] R. D. Maalihan, J. C. V. Aggari, A. S. Alon, R. B. Latayan, F. J. P. Montalbo, and A. D. Javier, "On the optimized fused filament fabrication of polylactic acid using multiresponse central composite design and desirability function algorithm," *Proceedings of the Institution of Mechanical Engineers, Part E: Journal of Process Mechanical Engineering*, vol. 240, no. 1, pp. 873–887, 2026, doi: 10.1177/09544089241247454.
[35] A. H. Kadhum, S. Al-Zubaidi, and S. S. Abdulkareem, "Effect of the infill patterns on the mechanical and surface characteristics of 3D printing of PLA, PLA+ and PETG materials," *ChemEngineering*, vol. 7, no. 3, Art. no. 46, 2023, doi: 10.3390/chemengineering7030046.